# Systems modeling reveals that store-operated calcium entry modulates force and fatigue during exercise

Emmet A. Francis[1,2], Juliette Hamid[1,*], Anusha Kumar[2,*], and Padmini Rangamani[1,2,**]

[1]Department of Pharmacology, University of California San Diego, La Jolla, CA, USA
[2]Department of Mechanical and Aerospace Engineering, University of California San Diego, La Jolla, CA, USA
[*]these two authors contributed equally to this work
[**]all correspondence may be addressed to prangamani@health.ucsd.edu

## Abstract

The dynamics of calcium ions ($Ca^{2+}$) in skeletal muscles link electrochemical activation and contractile force generation. An improved quantitative understanding of the mechanisms by which calcium dynamics modulate force production is crucial for optimizing muscle performance. Recent experimental data suggest that store-operated calcium entry (SOCE), the process of extracellular $Ca^{2+}$ influx upon depletion of $Ca^{2+}$ from the sarcoplasmic reticulum (SR), helps delay the onset of muscle fatigue. However, the mechanistic links between SOCE and sustained force generation in muscle remain unclear. We hypothesize that SOCE regulates force generation during sustained muscle activity by facilitating SR $Ca^{2+}$ store refilling. We test this hypothesis with a quantitative biophysical model that simulates the biochemical events of muscle contraction, from initial depolarization at the sarcolemma and T-tubules to $Ca^{2+}$ release from the SR to $Ca^{2+}$ binding and force generation throughout the myoplasm. We also consider the balance between $Ca^{2+}$ removal from the myoplasm and SOCE through the T-tubule membrane. We estimate the free parameters in the model by fitting them to experiments that measured sarcolemma membrane voltage and myoplasmic $Ca^{2+}$ transients in single muscle fibers in vitro. We then test the effects of SOCE inhibition on $Ca^{2+}$ dynamics and force production and find that the magnitude of myoplasmic calcium and force are significantly lower than in wild-type cells over repetitive stimuli. Finally, we predict the effects of varying the degree of SOCE inhibition during patterns of stimulus chosen to mimic those observed during resistance exercise or high-intensity interval training. These simulations predict a context-dependent relationship between force generation and SOCE, wherein increased SOCE is associated with greater force production during resistance exercise, but worsens the effects of fatigue in certain cases of high-intensity training.

## Introduction

Skeletal muscle fibers (myofibers) are responsible for generating force and supporting locomotion of the animal body. They are positioned at the mesoscale of the muscle hierarchy, between whole muscle composed of many fiber bundles (fascicles) and subcellular myofibrils consisting of aggregated thin and thick filaments [1, 2]. Contraction is initiated at the myofiber level - each fiber is stimulated by a motor neuron at the neuromuscular junction (NMJ). Understanding how myofibers integrate electrochemical inputs to initiate and sustain contraction is essential to dissecting muscle performance in different contexts, from peak performance to rapid fatigue.

The evolution of contractile force in a myofiber is largely governed by the pattern of input stimulus received from its motor neuron. This stimulus is provided mainly through acetylcholine (ACh) released into the synaptic cleft, which binds to its receptor in the myofiber membrane (sarcolemma) allowing an influx of positively charged ions [3]. The frequency of ACh release events determines the extent of fiber contraction, an example of the phenomenon known as rate encoding [4, 5]. At low frequencies, individual contractions (twitches) relax prior to the next stimulus, resulting in an overall low force generation. In contrast, at higher stimulus frequencies, twitches fuse into a single tetanic contraction, producing much higher forces. This provides one mechanism for modulating muscle force during different activities. Consequently, different exercises are characterized by different patterns of stimulus at the NMJ; for instance, electromyography (EMG) measurements revealed 10-60 Hz signals during resistance exercise [6] vs.

60-180 Hz signals during high-intensity interval training (HIIT) [7].

Following stimulation at the NMJ, force production itself is largely mediated by $Ca^{2+}$ elevations in the myoplasm. Initial depolarization of the sarcolemma leads to the opening of voltage-gated $Na^{+}$ channels, resulting in a full action potential that is conducted along the length of the fiber via the sarcolemma, and radially inwards through specialized membrane invaginations known as transverse tubules (T-tubules). In parallel, voltage-gated $Ca^{2+}$ channels such as the dihydropyridine receptor (DHPR) are activated, which allosterically couple to ryanodine receptors (RyRs) in the sarcoplasmic reticulum (SR) membrane to facilitate $Ca^{2+}$ release from the SR. Myoplasmic $Ca^{2+}$ then binds troponin on thin filaments, uncovering myosin binding sites to initiate cross-bridge cycling leading to myofiber contraction [8]. The rate of this contraction differs between fibers, broadly classified as fast-twitch (type II) or slow-twitch (type I) according to their protein composition, metabolism, and speed of contraction [1, 9]. Importantly, fast-twitch fibers are also more easily fatigued, in part due to rapid accumulation of phosphate in the myoplasm, reduced $Ca^{2+}$ release from the SR, and reduced myofibrillar $Ca^{2+}$ sensitivity [10–12].

Efficient contraction of muscle fibers relies on rapid transport of $Ca^{2+}$ into and out of the myoplasm. Accordingly, certain ATP-dependent membrane channels such as the plasma membrane $Ca^{2+}$ ATPase (PMCA) in the sarcolemma and T-tubules and sarco/endoplasmic reticulum ATPase (SERCA) in the SR membrane pump $Ca^{2+}$ back into the extracellular space or SR lumen, respectively. Due to the constant removal of some $Ca^{2+}$ from the cell, SR $Ca^{2+}$ levels are depleted over time in the absence of additional $Ca^{2+}$ entry through the sarcolemma. The phenomenon of store-operated $Ca^{2+}$ entry (SOCE) provides a natural solution to this problem by coupling SR $Ca^{2+}$ depletion to an additional influx through $Ca^{2+}$ channels in the plasma membrane [13, 14]. In short, stromal interaction molecule 1 (STIM1) in the SR membrane acts as a $Ca^{2+}$ sensor, binding SR $Ca^{2+}$ through its luminal domain [15, 16]. Following $Ca^{2+}$ dissociation from STIM1, it oligomerizes and then binds to the calcium channel Orai1 in the T-tubules, allowing $Ca^{2+}$ influx into the myoplasm [16, 17].

Although the importance of SOCE was originally appreciated in nonexcitable cells, many recent studies have uncovered its importance in excitable cells such as neurons, cardiomyocytes, and myofibers [18–23]. For instance, during exercise in wild-type mice, STIM1 and Orai1 channels were found to colocalize at the SR-T-tubule junction, functioning as $Ca^{2+}$ entry units (CEUs) [13, 19, 20]. CEUs have been proposed to facilitate rapid recovery of $Ca^{2+}$ within the fiber and delay the onset of fatigue [19, 20]. Indeed, muscles from dominant-negative Orai1 mice (dnOrai1) were more susceptible to fatigue and produced lower contractile force ex vivo [19]. However, other recent data suggests that SOCE can actually worsen fatigue; for example, one phosphoproteomics study identified that phosphorylation of STIM1 by AMP kinase (AMPK) both decreases SOCE and prevents fatigue [24].

Here, we seek to disentangle the effects of SOCE on force production in myofibers using a computational model. Such models have been instrumental in characterizing the complex mechanical, biochemical and electrical processes underlying muscle contraction [25, 26]. We present a novel multi-compartment $Ca^{2+}$ signaling model to test the hypothesis that SOCE facilitates prolonged force production and helps mitigate fatigue in fast-twitch skeletal muscle fibers. We first fit our model to experimental measurements of myoplasmic $Ca^{2+}$ and sarcolemma voltage in the literature, and then show that our model recapitulates measurements of $Ca^{2+}$ and force in SOCE-deficient myofibers. We then use our model to predict the role of SOCE for different patterns of stimuli chosen to mimic high-intensity exercise and resistance training. Our findings reconcile apparent contradictions in the literature, showing that the role of SOCE is context-dependent, often enhancing force production but, in certain cases, accelerating the onset of fatigue.

# Results

## Model Development

To investigate the impact of SOCE on calcium dynamics in skeletal muscle, we developed a well-mixed multi-compartment model of fast-twitch myofiber action potential generation and $Ca^{2+}$ dynamics. In our model, multiple excitation-contraction coupling and $Ca^{2+}$ signaling models were adapted to represent the behavior of the different ion channels and buffers [10, 25–27]. Rather than represent muscle signaling dynamics in full spatial detail, we adopted a compartmental approach, differentiating between junctional and bulk regions of each major compartment, including the myoplasm, SR, and extracellular space (Figure 1A). Junctional regions correspond to the volumes and surfaces at the triad, which consists of a T-tubule surrounded by two sections of the SR on either side (terminal cisternae). We did not consider propagation of electrochemical signals along the length of the fiber, and we assumed that the action potential propagates into the T-tubules much faster than other events in our model. Throughout,

we differentiate between each subcompartment using subscripts for clarity; for instance, $Ca^{2+}$ concentration in the junctional myoplasm is written as $[Ca^{2+}]_{myo,junc}$.

Our overall model is divided into 4 modules, including action potential generation (Module 1, Figure 1B), $Ca^{2+}$ influx and release (Module 2, Figure 1C), $Ca^{2+}$ binding events and cross-bridge cycling (Module 3, Figure 1D), and $Ca^{2+}$ removal and SOCE (Module 4, Figure 1E). The complete model consists of a system of 51 ordinary differential equations (ODEs), including flux balance equations and equations governing changes in receptor or channel state. We briefly summarize each module below, with a more detailed description provided in Methods and Supplementary Information (Tables S3 to S7).

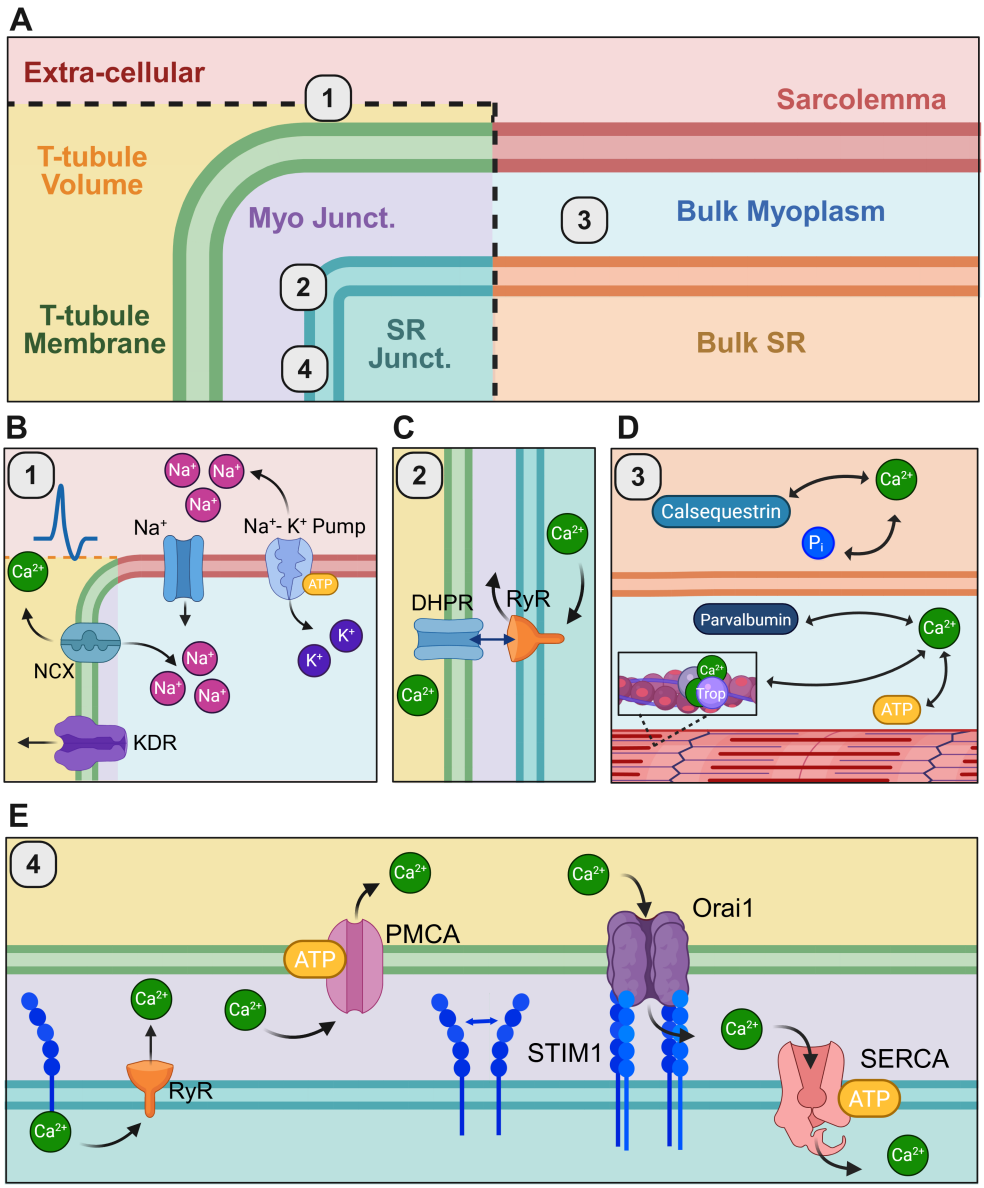


**Figure 1: Schematic for model components of myofiber $Ca^{2+}$ signaling.** A) A subregion of the cross-section of the muscle fiber is divided into compartments, each labeled with different colors. Ions freely diffuse between bulk and junctional regions of each compartment, separated by black dashed lines here. B-D) The sequence of signaling events directly correlated to force generation are grouped into four modules. In module 1, the applied current triggers an action potential through $Na^+$ and $K^+$ fluxes (B). In module 2, action potential propagation leads to DHPR-RyR interactions, triggering $Ca^{2+}$ release from the SR (C). In module 3, $Ca^{2+}$ binds to proteins and induces the cross-bridge cycle, producing contractile force (D). In module 4, $Ca^{2+}$ unbinds from STIM1 during SR depletion, causing STIM1 to oligomerize and form complexes with Orai1, allowing $Ca^{2+}$ influx from the extracellular space into the myoplasm (E).

### Module 1: Action potential generation

Action potentials are modeled using a Hodgkin-Huxley-type formulation, in line with previous models developed for mammalian skeletal muscle [10, 25, 26, 28] (Figure 1B). Briefly, we consider $Na^+$ current through a voltage-gated $Na^+$ channel ($I_{Na^+}$), followed by $K^+$ efflux through the $K^+$ delayed rectifier ($I_{KDR}$), governed by equations from [25]. We also include currents through the $K^+$ inward rectifier ($I_{KIR}$), which helps to maintain the resting potential of the membrane [29], and the $Na^+$-$K^+$ pump ($I_{Na^+\text{-}K^+}$), which restores gradients in $Na^+$ and $K^+$ across the sarcolemma [25]. Other secondary currents include $Na^+$ import through the $Na^+$-$Ca^{2+}$ exchanger ($I_{NCX}$) and a $Cl^-$ current ($I_{Cl^-}$) that regulate the resting membrane potential. Altogether, this results in total ionic currents through the T-tubule membrane (subscript TT) and bulk sarcolemma (subscript SL):

$$\begin{aligned} I_{\text{ionic,TT}} = \; & 0.1 I_{Na^+,TT} + 0.1 I_{Na^+\text{-}K^+,TT} + I_{NCX,TT} + \\ & 0.45 I_{KDR,TT} + I_{KIR,TT} + 0.1 I_{Cl^-,TT} + I_{Ca^{2+},TT}, \end{aligned} \tag{1}$$

$$\begin{aligned} I_{\text{ionic,SL}} = \; & I_{Na^+,SL} + I_{Na^+\text{-}K^+,SL} + I_{NCX,SL} + I_{KDR,SL} + \\ & I_{KIR,SL} + I_{Cl^-,SL} + I_{Ca^{2+},SL}, \end{aligned} \tag{2}$$

where $I_{Ca^{2+},TT}$ and $I_{Ca^{2+},SL}$ are additional $Ca^{2+}$ currents defined in Module 4. Full expressions for each current are given in Table S5 and their relative contribution at T-tubules vs. sarcolemma are summarized in Table S3. Balancing these ionic currents with a capacitive current at the sarcolemma and considering conductivity between the sarcolemma and T-tubules yields:

$$\frac{dV_{SL}}{dt} = \frac{SA_{SL} I_{\text{ionic,SL}} + I_{SL} - I_{\text{SL-TT}}}{SA_{SL} C_M}, \tag{3}$$

$$\frac{dV_{TT}}{dt} = \frac{SA_{TT} I_{\text{ionic,TT}} + I_{\text{SL-TT}}}{SA_{TT} C_M}, \tag{4}$$

where $SA_{SL}$ is the surface area of the sarcolemma, $SA_{TT}$ is the surface area of the T-tubules, $C_M$ is the specific membrane capacitance, and $I_{SL}$ is the stimulus current through the sarcolemma. This stimulus was modeled as square waves with a pulse width of 1 ms. $I_{\text{SL-TT}}$ is the current from the sarcolemma into the T-tubule membrane, calculated as in [25]:

$$I_{SL\text{-}TT} = SA_{SL} \frac{V_{TT} - V_{SL}}{R_a}, \tag{5}$$

where $R_a$ is the access resistance at the entrance to the T-tubules.

### Module 2: $Ca^{2+}$ release

$Ca^{2+}$ release from the SR occurs in the junctional region upon a sufficient increase in T-tubule membrane voltage. The L-type $Ca^{2+}$ channel, the DHPR, acts as a voltage sensor in the T-tubule membrane, allosterically interacting with the ryanodine receptor (RyR) in the SR membrane and leading to its opening. In line with previous literature, we assume that the $Ca^{2+}$ flux through DHPR itself is negligible and it mainly serves as a voltage sensor to gate the RyR [30].

The resulting flux through the RyR is given by:

$$J_{RyR} = \nu_{\text{max,RyR}} P_{\text{O,RyR}} ([Ca^{2+}]_{\text{SR,junc}} - [Ca^{2+}]_{\text{myo,junc}}), \tag{6}$$

where $\nu_{\text{max,RyR}}$ is the maximum permeability of the RyR and $P_{\text{O,RyR}}$ is the open probability of the RyR governed by $Ca^{2+}$ concentration and TT membrane voltage. The voltage dependence of $P_{\text{O,RyR}}$ is dictated by a 10-state Monod, Wyman, and Changeux (MWC)-type model (as in [31]) and the $Ca^{2+}$ dependence captures slow deactivation, as introduced by Senneff and Lowery [26] (see expressions in Table S5).

### Module 3: $Ca^{2+}$ binding

Many proteins in the myoplasm and SR act as $Ca^{2+}$ buffers, such that the total $Ca^{2+}$ in either compartment is much higher than the free $Ca^{2+}$ [32–34]. In the myoplasm, we consider $Ca^{2+}$ binding to parvalbumin, ATP, and troponin, in addition to competitive binding of $Mg^{2+}$ to parvalbumin and ATP [10, 26, 35, 36] In the SR lumen, we account for $Ca^{2+}$ binding to calsequestrin [10, 26, 27].

Additionally, $Ca^{2+}$ binding to troponin on the thin filament in the bulk myoplasm leads to cross-bridge cycling. In short, two $Ca^{2+}$ ions bind to a single troponin complex, causing tropomyosin to change shape and expose myosin binding sites on the thin filament [1, 8, 10]. To model this, we introduce a six-state cross-bridge cycling model, modified from the eight-state model utilized by Shorten et al [10] as detailed in Tables S5 and S6 and shown in Figure S1. The production of contractile force is assumed to evolve with changes in the density of cross-bridges in a post-powerstroke (force-generating) conformation $A_{post}$:

$$\frac{d[A_{\text{Post}}]}{dt} = h_0[A_{\text{Pre}}] - g_0[A_{\text{Post}}][\text{ATP}]_{\text{myo,bulk}} - h_p[A_{\text{Post}}][P_i]_{\text{myo,bulk}}, \tag{7}$$

where $h_0$ is the power stroke rate, $g_0$ is the rate of myosin head detachment post-power stroke, and $h_p$ is the reverse rate to the pre-power stroke conformation. In the above relationship, we explicitly assume that reactions depend on concentrations of ATP and inorganic phosphate according to mass action, an effect neglected in some previous models [10, 26]. The dependence of power stroke reversal on phosphate has been particularly suggested as an important regulator of fatigue [12].

We track the consumption of ATP and release of phosphate due to cross-bridge cycling and activity of ion pumps and other intracellular processes. To avoid depletion of ATP at steady-state, we introduce an empirical ATP production term (Table S5). Phosphate is also allowed to move into the SR and conditionally form a $Ca^{2+}$-phosphate precipitate in line with previous work [10, 37, 38]. This reduces the SR $Ca^{2+}$ available for rapid release, providing an additional mechanism for phosphate-mediated fatigue.

### Module 4: $Ca^{2+}$ removal and SOCE

$Ca^{2+}$ homeostasis relies on rapid removal from the myoplasm via ATP-dependent fluxes through the plasma membrane $Ca^{2+}$ ATPase (PMCA) into the extracellular space and sarco/endoplasmic reticulum $Ca^{2+}$ ATPase (SERCA) into the SR lumen. We represent these fluxes phenomenologically using first-order Hill equations that depend on both $Ca^{2+}$ concentration and ATP concentration (Table S5). $Ca^{2+}$ is additionally passively transported from the myoplasm to the extracellular space through NCX, as dictated by $J_{NCX}$ (proportional to $I_{NCX}$ in Equations (1) and (2)).

Given that not all $Ca^{2+}$ released from the SR is pumped back in through SERCA, SOCE is required to restore SR $Ca^{2+}$ levels following rapid depletion. Here, we draw from previous work across several cell types [16, 21, 39, 40] to mathematically describe SOCE in skeletal muscle.

The SR luminal domain of STIM1 binds SR $Ca^{2+}$, allowing it to act as a $Ca^{2+}$ sensor [15]. Upon depletion of SR $Ca^{2+}$, $Ca^{2+}$ unbinding leads to STIM1 oligomerization and binding to Orai1 channels at SR-T-tubule junctions [16]. Orai1 channels are tetramers with four binding sites for STIM1 dimers [16, 39]. Previous experimental measurements [15, 17] establish a relationship between SOCE conductance and SR $Ca^{2+}$ that is well-represented by a Hill equation with a coefficient close to 4, utilized by multiple previous models [21, 23, 40]. Accordingly, we model the steady-state open probability of Orai1 channels, $P_{\text{O,Orai1},\infty}$, as:

$$P_{\text{O,Orai1},\infty} = \frac{1}{1 + \left(\frac{[\text{Ca}^{2+}]_{\text{SR,junc}}}{K_{\text{STIM1}}}\right)^4}, \tag{8}$$

where $K_{\text{STIM1}}$ is an equilibrium constant dictating the junctional SR $Ca^{2+}$ concentration at which SOCE is at half maximal activation. We expect the system to approach this steady state over some characteristic time $\tau_{SOCE}$ required for STIM1 oligimerization, diffusion, and binding with Orai1 to form CEUs [16]:

$$\frac{dP_{\text{O,Orai1}}}{dt} = \frac{P_{\text{O,Orai1},\infty} - P_{\text{O,Orai1}}}{\tau_{\text{SOCE}}}. \tag{9}$$

This minimal approach allows us to represent SOCE without introducing a large number of new free parameters. The $Ca^{2+}$ flux due to SOCE is assumed to be restricted to the junctional region and is calculated as:

$$J_{\mathrm{SOCE}} = P_{\mathrm{O,Orai1}} g_{\mathrm{Orai1}} \frac{N_A}{2F} (E_{\mathrm{Ca^{2+},junc}} - V_{\mathrm{TT}}), \tag{10}$$

where $g_{\mathrm{Orai1}}$ is the Orai1 conductance, $N_A$ is Avogadro's number, and $F$ is Faraday's constant. $E_{\mathrm{Ca^{2+},junc}}$ is the Nernst potential for $Ca^{2+}$ across the T-tubule membrane:

$$E_{\mathrm{Ca^{2+},junc}} = \frac{RT}{2F} \ln \left( \frac{[\mathrm{Ca^{2+}}]_{\mathrm{TT}}}{[\mathrm{Ca^{2+}}]_{\mathrm{myo,junc}}} \right), \tag{11}$$

where $R$ is the gas constant and $T$ is the temperature.

The fluxes outlined in Modules 2-4 allow us to write ODEs for $Ca^{2+}$ in each region of the myoplasm and the SR. Furthermore, we compute the additional $Ca^{2+}$ fluxes through the T-tubule membrane and bulk sarcolemma introduced in Equations (3) and (4):

$$I_{\mathrm{Ca^{2+},TT}} = \frac{2F}{N_A} \left( J_{\mathrm{SOCE}} + J_{\mathrm{Ca^{2+},TT\ leak}} - J_{\mathrm{PMCA}} \right), \tag{12}$$

$$I_{\mathrm{Ca^{2+},SL}} = \frac{2F}{N_A} \left( J_{\mathrm{Ca^{2+},SL\ leak}} - J_{\mathrm{PMCA}} \right), \tag{13}$$

where $J_{\mathrm{Ca^{2+},TT\ leak}}$ and $J_{\mathrm{Ca^{2+},SL\ leak}}$ are leak fluxes through the T-tubule membrane and sarcolemma, respectively.

Most species in the model exist in both junctional and bulk regions, with the exception of $P_{\mathrm{O,Orai1}}$ (T-tubules only) and all cross-bridge related variables (bulk myoplasm only). Furthermore, concentrations of ions are tracked within the T-tubule volume, but extracellular ion concentrations are assumed constant (see Figure 1A for clearly annotated regions).

## Calibrated model recapitulates dynamics of membrane potential and myoplasmic $Ca^{2+}$

Our model utilizes a unique combination of channels and receptors not combined in previous models; accordingly, while we used initial parameter estimates from the literature, it was necessary to formally estimate best-fit values for each parameter. Excluding geometric parameters, there are 106 free parameters Table S7 in the model. We first conducted a global Morris sensitivity analysis to identify the most influential parameters in the model [43]. As quantities of interest (QOIs), we considered the maximum and time-averaged values of the myoplasmic $Ca^{2+}$ concentration and sarcolemma voltage over a single excitation event. Myoplasmic $Ca^{2+}$ was defined as a weighted average by volume:

$$[\mathrm{Ca^{2+}}]_{\mathrm{avg}} = \frac{[\mathrm{Ca^{2+}}]_{\mathrm{myo,junc}} vol_{\mathrm{myo,junc}} + [\mathrm{Ca^{2+}}]_{\mathrm{myo,bulk}} vol_{\mathrm{myo,bulk}}}{vol_{\mathrm{myo,junc}} + vol_{\mathrm{myo,bulk}}}. \tag{14}$$

Morris sensitivity analysis was used to identify several of the most influential parameters for $Ca^{2+}$ and voltage dynamics (Figure 2A-B, Figure S2). Sarcolemma voltage was most sensitive to parameters associated with the $Na^+$ channel ($V_m$, $V_h$, $V_{S\infty}$; refer to Table S7) and the $K^+$ delayed rectifier ($V_n$), in agreement with previous work [10, 25]. $Ca^{2+}$ dynamics were most sensitive to parameters related to $Na^+$ channel activity ($V_m$, $V_h$, $Ca^{2+}$ export through PMCA ($g_{\mathrm{PMCA}}$), and currents through the $Na^+$-$Ca^{2+}$ exchanger ($k_{\mathrm{sat,NCX}}$).

We proceeded to estimate parameters in two stages, as fully described in Methods. Briefly, we first fit the model to measurements of membrane potential [41], only varying the 28 parameters with greater than 10% sensitivity with respect to average and/or peak voltage (Figure S2A-B). Then, starting from these parameters as initial estimates and allowing all other parameters to vary, we simultaneously fit our model to voltage and to myoplasmic $Ca^{2+}$ data collected from multiple papers that conducted fluorescence or voltage measurements in single mouse fast-twitch myofibers [36, 40, 41]. Overall, the fitting process results in a strong match with all the experiments considered (Figure 2C-E).

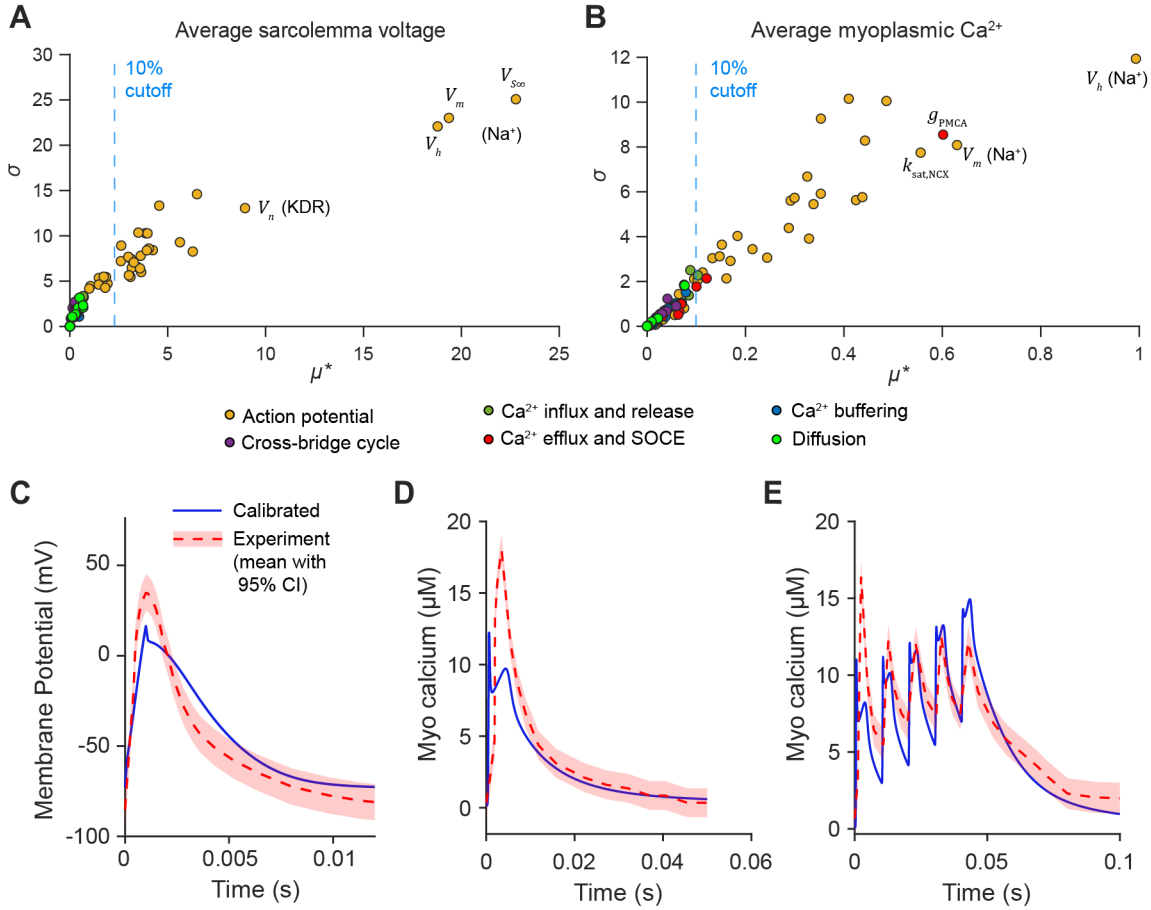


**Figure 2: Sensitivity analysis and model calibration.** A, B) Results from Morris sensitivity analysis of average sarcolemma voltage (A) and average $[Ca^{2+}]_{myo}$ (B) as QOIs. The horizontal axis displays the absolute value of the mean, $\mu^*$, and the vertical axis shows the standard deviation, $\sigma$, of elementary effects. The parameters with the four highest values of $\mu^*$ are labeled individually. C) Results of model calibrated to experimental membrane potential measurements [41] (C) and to $[Ca^{2+}]_{myo}$ dynamics data for a single pulse stimulus (D) [36] or a train of five stimulus pulses at 100 Hz (E) [40]. All experimental data were extracted from source papers using PlotDigitizer [42]. Conditions were varied according to extracellular buffer and temperature in each experiment. [41]: $[Na^+]_{EC} = 1.18 \times 10^5$ µM, $[K^+]_{EC} = 5.33 \times 10^3$ µM, $[Cl^-]_{EC} = 1.26 \times 10^5$ µM, $[Ca^{2+}]_{EC} = 1.80 \times 10^3$ µM, $T = 295.15$ K; [36]: $[Na^+]_{EC} = 1.50 \times 10^5$ µM, $[K^+]_{EC} = 2.00 \times 10^3$ µM, $[Cl^-]_{EC} = 1.58 \times 10^5$ µM, $[Ca^{2+}]_{EC} = 2.00 \times 10^3$ µM, $T = 293.15$ K; [40]: $[Na^+]_{EC} = 1.38 \times 10^5$ µM, $[K^+]_{EC} = 3.90 \times 10^3$ µM, $[Cl^-]_{EC} = 1.44 \times 10^5$ µM, $[Ca^{2+}]_{EC} = 1.00 \times 10^3$ µM, $T = 295.15$ K.

We then examined the baseline predicted behavior of our model in terms of membrane voltage, $Ca^{2+}$, and contractile force (Figure 3). In response to a 100 Hz stimulus (Figure 3A), we observed consistent action potentials that match the characteristic shape of a skeletal muscle action potential, starting at a resting voltage close to -80 mV and rising to a peak of about 20 mV (Figure 3B). Simultaneously, $Ca^{2+}$ accumulates within the myoplasm (Figure 3C), leading to increases in contractile force as indicated by the relative density of post-power stroke cross-bridges (Figure 3D). As expected for this high-frequency stimulus, individual contractile events (twitches) fuse and rapidly approach maximum activation, corresponding to tetanic contraction.

We also dissected these events in terms of their constitutive currents and fluxes (Figure 4). Membrane depolarization leads to $Na^+$ channel opening in the T-tubules and sarcolemma, followed by opening of the $K^+$ delayed rectifier during repolarization (Figure 4A). The $Na^+$-$K^+$ pump counteracts these fluxes to restore the resting gradients of both ions, while other small currents through the $Na^+$-$Ca^{2+}$ exchanger and the $K^+$ inward rectifier play secondary roles (Figure 4A). In parallel, depolarization triggers activation of DHPRs in the T-tubules, which allosterically interact with RyRs in the junctional SR membrane to trigger their opening (Figure 4B). This large $Ca^{2+}$ release through RyRs is the dominant source for $Ca^{2+}$ elevations in the myoplasm and results in higher concentrations in the junctional compartment compared to the bulk myoplasm (Figure S3). Myoplasmic $Ca^{2+}$ then decreases due to binding to buffers (ATP, parvalbumin, troponin) and removal to the extracellular and SR spaces through PMCA and SERCA, respectively (Figure 4B). During this phase of store refilling, we observed a concomitant increase in SOCE, but $J_{\mathrm{SOCE}}$ remained small compared to other $Ca^{2+}$ fluxes in the model.

## SOCE facilitates sustained calcium elevations

Having established the agreement between our baseline model and the physiological signaling events in skeletal muscle fibers, we systematically examined the importance of SOCE for $Ca^{2+}$ dynamics and force production. As initial validation of our simplified mathematical treatment of SOCE, we simulated treatment of cells with the SERCA inhibitor, thapsigargin (TG), commonly used to assess SOCE across cell types [16, 17, 24, 44]. In this experiment, cells are placed in $Ca^{2+}$-free media and then treated with TG, causing $Ca^{2+}$ to leak from the SR into the myoplasm and slowly exit the cell due to efflux through PMCA. Upon reintroducing $Ca^{2+}$ to the media, a large store-operated $Ca^{2+}$ influx occurs. Our computational version of this experiment recapitulated measurements of store-operated $Ca^{2+}$ fluxes observed across cell types [16, 24] (Figure 5A).

We then considered stimulation of a myofiber at 100 Hz with and without SOCE. Initial tests predicted implausibly high levels of myoplasmic $Ca^{2+}$ within 1 s of repetitive stimuli (up to 50 μM). We postulated this was due to the simplified, well-mixed assumptions of our model. In reality, additional time is required for $Ca^{2+}$ to diffuse not only from the junctional to bulk myoplasmic regions, but throughout the bulk region itself. We phenomenologically represented this effect by reducing the effective diffusion coefficient of ions between the junctional and bulk regions ($D_{\mathrm{ion}}$) to 10% of its original value. We then found that SOCE regulation played a significant role in $Ca^{2+}$ dynamics. While myofibers with a baseline value of SOCE conductance showed dynamics similar to simulations without SOCE, increasing Orai1 conductance by a factor of 20 led to a 15% increase in peak myoplasmic $Ca^{2+}$ (Figure 5B). This increased SOCE conductance remains physiologically relevant, as the assembly of CEUs during exercise is expected to significantly enhance $Ca^{2+}$ flux through Orai1 [20].

Finally, we examined the contractile force exerted by fibers with and without SOCE. While the predicted dynamics of contractile force were similar in both cases, we did observe a 3.6% increase in the maximum relative force for cells with strong (20×) SOCE conductance over cells with no SOCE. Furthermore, in both cases, contractile force declines after less than 1 s of stimulation. This effect is largely mediated by phosphate accumulation in the myoplasm (Figure S4), in line with the established role of phosphate in muscle fatigue [10–12, 45].

## SOCE modulates contractile force in a frequency-dependent manner

Our initial simulations suggest that SOCE is an important regulator of $Ca^{2+}$ dynamics and force production in skeletal muscle. We then used our model to predict force as a function of stimulus frequency, a relevant consideration in the context of exercise. We considered a case previously tested experimentally, in which dominant-negative Orai1 (dnOrai1) mouse EDL muscle exhibited frequency-dependent inhibition of force generation [19]. In keeping with experiments, we considered different frequencies of stimuli consisting of square-wave pulse trains for a total of 0.5 s each.

At low stimulus frequencies (less than 20 Hz), we observed very little force production regardless of SOCE, as tetani remain unfused (Figure 6A). However, SOCE consistently enhances force production by a small amount at

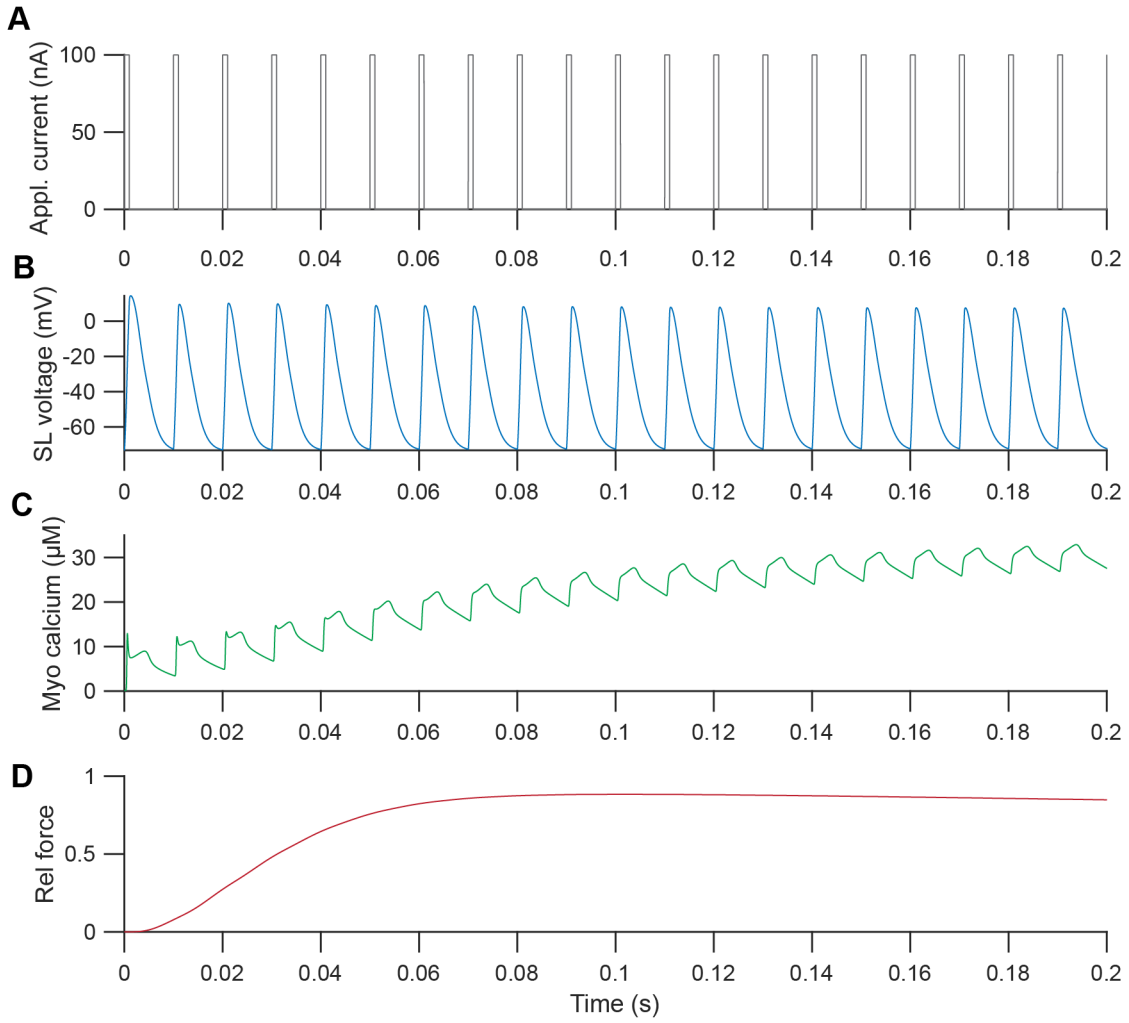


**Figure 3: Model output for membrane potential and $Ca^{2+}$ dynamics at 100 Hz stimulus.** Input 100 Hz square wave current at the bulk sarcolemma (A) gives rise to action potentials in the sarcolemma (SL) (B) and subsequent increases in myoplasmic $Ca^{2+}$ (C). Binding of $Ca^{2+}$ to troponin leads to cross bridge cycling, manifesting as contractile force (D). Relative force is defined as the concentration of post-power stroke cross-bridges relative to their concentration at saturating $Ca^{2+}$ concentrations.

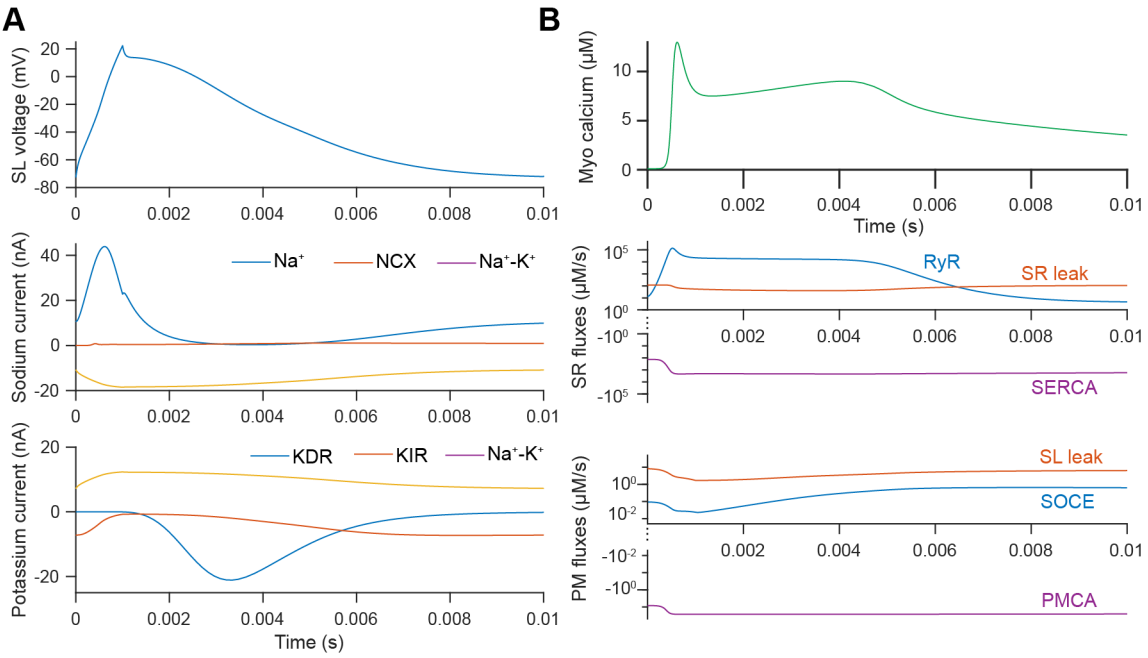


**Figure 4: Currents and $Ca^{2+}$ fluxes during the first action potential of a train.** A) Sarcolemma depolarization and repolarization (upper) coincide mainly with an inward $Na^+$ current (middle) and outward $K^+$ delayed rectifier (KDR) current (lower), respectively. Currents through the $Na^+$-$K^+$ pump, $Na^+$-$Ca^{2+}$ exchanger (NCX), and $K^+$ inward rectifier (KIR) are also plotted for reference. B) $Ca^{2+}$ transient driven by the initial action potential (upper) is decomposed into fluxes through the SR membrane (middle) and cell membrane (SL and TT; lower). Release through RyR and reuptake into the SR through SERCA are the dominant fluxes.

moderate to high stimulus frequencies (Figure 6B-C). However, our tests did not reproduce the fast decline in force over time observed in experiments with dnOrai1 muscle at higher frequencies (greater than 100 Hz), and our simulations generally overestimated contractile force in SOCE knockout fibers at high frequencies (Figure 6C-D). This suggests that additional SOCE-regulated processes not considered in our model may contribute at higher stimulus frequencies. As one possible mechanism, we considered that SOCE might modulate the resting levels of phosphate in the myoplasm, perhaps through regulation of mitochondrial fission and fusion [46] (see Discussion). Upon increasing the resting concentration of myoplasmic phosphate by 50%, we effectively rescued the behavior measured in experiments (Figure 6C-D).

## Computational predictions suggest context-dependent role of SOCE in different forms of exercise

Finally, we considered the predictions of our model for different frequencies and patterns of stimuli relevant to different forms of exercise; in particular, resistance exercise and high-intensity interval training (HIIT). These exercises have previously been characterized by different frequencies and duration of stimuli, with frequencies from 10-50 Hz for resistance exercise [6] and 60-180 Hz for HIIT [7]. During high-intensity exercise such as sprinting, stimulus of a given muscle occurs in discrete phases during each stride. Considering data from muscles that have high abundance of fast twitch fibers (gastrocnemius medialis or the gastrocnemius lateralis) [47], we assumed that stimulus occurs over a 0.1625 s time interval for each 0.65 s stride, with a stimulus frequency of 100 Hz. Resistance exercise was modeled after the isometric contraction measured in the quadriceps in previous work, consisting of 3 s of contraction followed by 3 s of rest, with a stimulus frequency of 40 Hz [6]. In the following tests, we considered stimulus trains designed to mimic 20 s of running or 10 repetitions (60 s total) of resistance exercise.

To examine potential roles for SOCE in exercise, we varied SOCE conductance ($g_{\mathrm{Orai1}}$) and STIM1 $Ca^{2+}$ sensitivity ($K_{\mathrm{STIM1}}$) over a wide range of values (0.1 to 100 times baseline for $g_{\mathrm{Orai1}}$, 0.3 to 3 times for $K_{\mathrm{STIM1}}$. Shifts in $g_{\mathrm{Orai1}}$ can be attributed changes in SR/T-tubule organization [20], transport of STIM1 [48, 49], or Orai receptor turnover [50]. On the other hand, changes in $K_{\mathrm{STIM1}}$ may be associated with biochemical modifications that alter STIM1-Orai1 binding, STIM1 autoinhibition, or STIM1-$Ca^{2+}$ binding. For instance, phosphorylation of STIM1

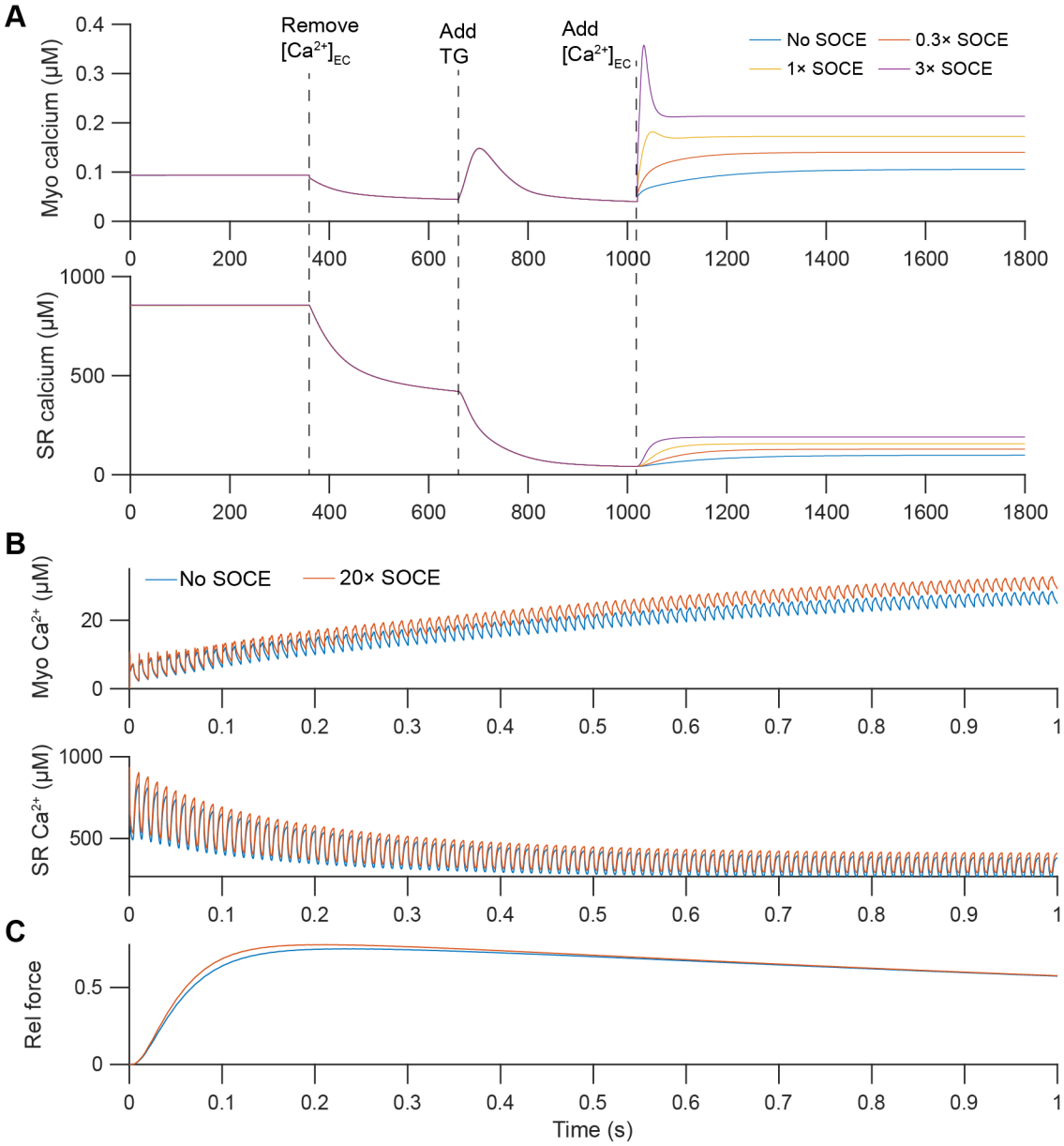


**Figure 5: Predicted effects of SOCE in computational experiments.** A) Predicted myoplasmic (upper) and SR (lower) $Ca^{2+}$ dynamics in response to a conventional thapsigargin (TG) assay, modeled after tests in [24]. Extracellular $Ca^{2+}$ is initially 1300 μM, then reduced to 0 μM at $t = 360$ s (e.g., via addition of a $Ca^{2+}$ chelator such as EGTA). Addition of thapsigargin at $t = 660$ s reduces SERCA activity to 10% of its resting activity, inducing $Ca^{2+}$ release from the SR. Extracellular $Ca^{2+}$ (1300 μM) is then reintroduced at $t = 1020$ s, triggering SOCE, with Orai1 conductance varied relative to the estimated value in Table S7. B) Predicted myoplasmic (upper) and SR (lower) $Ca^{2+}$ dynamics in response to 100 Hz stimulus with high SOCE (20 times baseline estimated conductance) vs. no SOCE, $0.1D_{ion}$. C) Predicted relative contractile force for conditions in panel B shown in panel B.

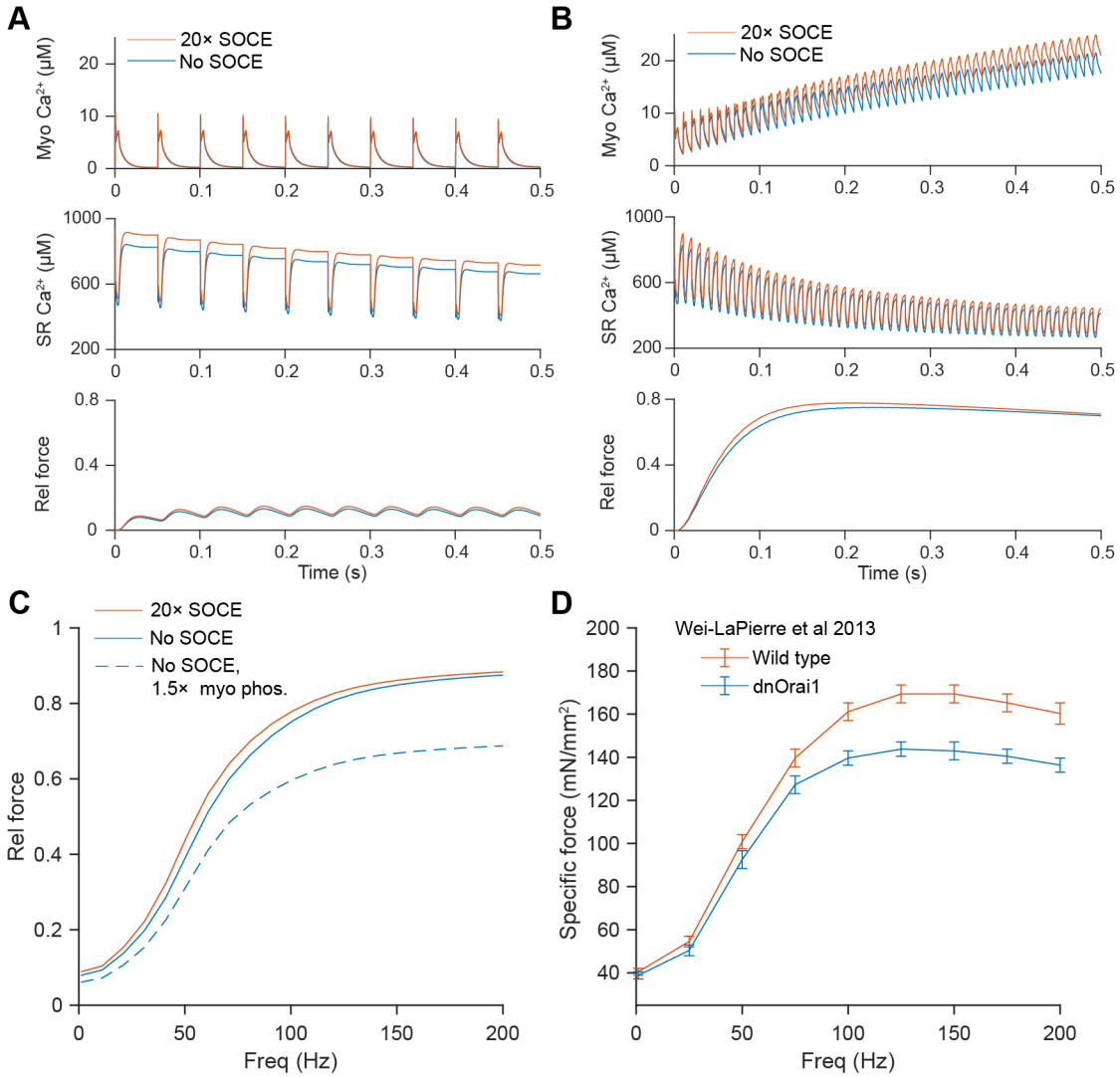


**Figure 6: Frequency-dependent force generation with vs. without SOCE.** A-B) Predicted effects of SOCE on myoplasmic $Ca^{2+}$, SR $Ca^{2+}$, and contractile force are plotted for 20 Hz (A) and 100 Hz (B) stimuli. C) Frequency-dependent maximum contractile force with vs. without SOCE, or with no SOCE and higher levels (1.5×) of resting myoplasmic phosphate. D) Experimental measurements of maximum force during in vitro testing of muscle from the EDL of wild type or dominant negative Orai1 (dnOrai) mice [19]. $n = 14$ for both wild type and dnOrai1 conditions and error bars denote standard error of the mean. Data were extracted from the original figure using manual analysis in ImageJ.

by AMPK has been shown to bias STIM1 towards a folded, autoinhibited conformation [24]. This is expected to decrease $K_{\mathrm{STIM1}}$ (see Supplementary Information); that is, phosphorylated STIM1 requires further depletion of SR $Ca^{2+}$ prior to binding to Orai1 and inducing $Ca^{2+}$ influx. In parallel with these SOCE-related parameters, we varied the troponin $Ca^{2+}$ sensitivity ($k_{\mathrm{on,trop}}$) and phosphate degradation rate ($k_{\mathrm{phos,deg}}$) to dissect how the effects of SOCE depend on other important factors in the model (Figures S5 and S6).

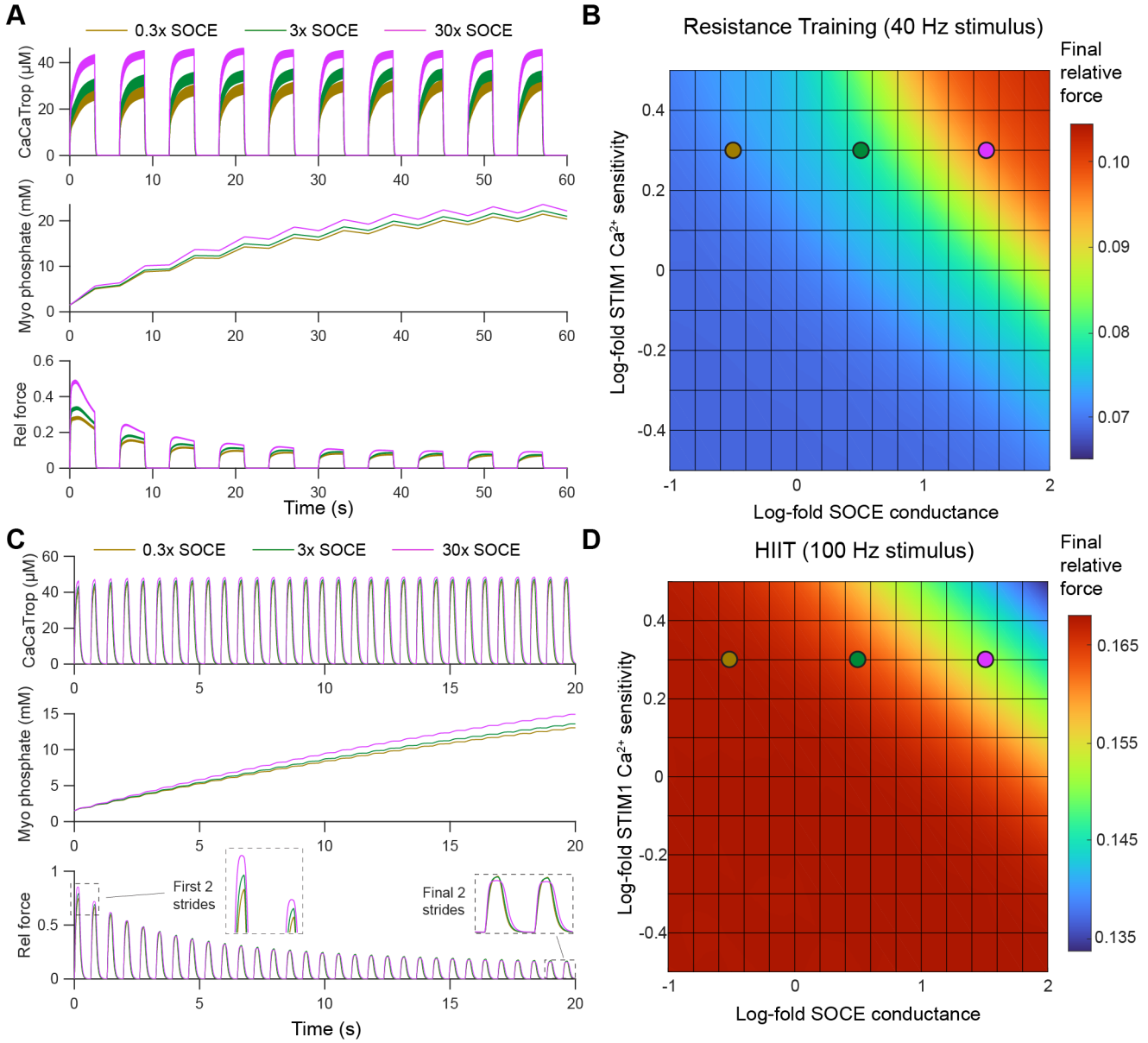


**Figure 7: Predicted effects of SOCE in different exercise regimes.** A) Predicted dynamics of [Trop-2$Ca^{2+}$], myoplasmic phosphate, and force over time during patterns of 40 Hz stimuli designed to mimic vastus lateralis activity during resistance training [6]. B) Phase diagram summarizing the maximum contractile force during the final repetition of a 10-repetition resistance training set running interval as a function of $K_{\mathrm{STIM1}}$) and $g_{\mathrm{Orai1}}$. C) Predicted dynamics of [Trop-2$Ca^{2+}$], myoplasmic phosphate, and force over time during patterns of 100 Hz stimuli designed to mimic gastrocnemius medialis activity during running [47]. D) Phase diagram summarizing the maximum contractile force during the final stride of a 20 s running interval as a function of STIM1 $Ca^{2+}$ sensitivity ($K_{\mathrm{STIM1}}$) and SOCE conductance ($g_{\mathrm{Orai1}}$). Tests in panels A and C are conducted for low (0.3×), moderate (3×), and high (30×) SOCE conductance at $2\times K_{\mathrm{STIM1}}$, as indicated by points on the phase diagrams in panels B and D. All tests shown here used baseline estimated values for $k_{\mathrm{on,T1}}$ and $k_{\mathrm{phos,deg}}$, with $0.1D_{\mathrm{ion}}$.

We found that force production is enhanced by elevating SOCE conductance during resistance exercise (Figure 7A-B). Mechanistically, these higher forces are attributed to a significantly higher fraction of troponin binding to $Ca^{2+}$ in the myoplasm, allowing for faster crossbridge cycling despite increased accumulation of myoplasmic phosphate

(Figure 7A). This effect is tuned by STIM1 $Ca^{2+}$ sensitivity and SOCE conductance, with the largest effects on force observed upon increasing both parameters (Figure 7B). Phosphate degradation rate mainly determines the extent of force reduction (fatigue) during the simulation, whereas troponin $Ca^{2+}$ sensitivity dictates the relative increase in force due to SOCE (Figure S5).

Surprisingly, in certain cases increased SOCE reduces the force produced at the end of a 20-second HIIT stimulus (Figure 7C-D). Specifically, when troponin $Ca^{2+}$ sensitivity is high, elevated SOCE accelerates the onset of fatigue (Figure S6). At this higher stimulus frequency compared to resistance exercise (100 Hz vs. 40 Hz), myoplasmic $Ca^{2+}$ and the resulting fraction of troponin bound to $Ca^{2+}$ are high regardless of SOCE (Figure 7C). Therefore, increased accumulation of myoplasmic phosphate for high SOCE (high conductance or high $K_{\mathrm{STIM1}}$) is detrimental, resulting in lower contractile force compared to low SOCE by the end of the simulation (Figure 7C-D). Thus, while increased SOCE often improves force output, very high rates of $Ca^{2+}$ entry can worsen fatigue in some cases, revealing a nuanced, context-dependent role for SOCE in excitation-contraction coupling in skeletal muscle.

# Discussion

Given the well-established role of $Ca^{2+}$ release in skeletal muscle contraction, understanding conditions that optimize $Ca^{2+}$ release and contractile force generation in exercise, and how such factors contribute to muscle failure in fatigue is important for establishing predictive relationships between calcium dynamics and athletic performance. Here, we investigate the particular role of store-operated $Ca^{2+}$ entry in excitation-contraction coupling in skeletal muscle. While many recent experimental studies had suggested a central role of SOCE in enhancing force and mitigating fatigue [19, 20], a majority of the existing computational models of excitation-contraction coupling in skeletal muscle did not include this important pathway. Our model not only addresses this gap in the literature but combines action potential machinery with detailed $Ca^{2+}$ handling, constrains model parameters to experimental data, and generates testable predictions about the impact of SOCE on fatigue in skeletal muscle.

Our model predicts that SOCE can significantly enhance elevations in myoplasmic $Ca^{2+}$ and contractile force, in line with our original hypothesis (Figures 5 and 6). However, in contrast to our initial expectations, we found that this relationship was not consistent across all parameter regimes, which helps resolve an apparent contradiction in the current literature regarding SOCE in skeletal muscle. Multiple studies have measured reduced force and increased susceptibility to fatigue in SOCE-deficient mice [19, 51]. In contrast, recent data suggests that SOCE deficiency might actually mitigate fatigue in certain cases [24]. Here, we show that these two effects can be understood as the outcomes of the same biophysical system operating in different regimes. At lower stimulus frequencies or higher rates of phosphate clearance, we predict that SOCE enhances $Ca^{2+}$ levels, leading to increased contractile force. However, at high-frequency stimulus and slow phosphate clearance, increased SOCE is associated with higher rates of ATP hydrolysis, leading to accumulation of phosphate in the myoplasm. In this case, reducing SOCE mitigates fatigue, in agreement with experiments that show silencing STIM1 or inhibiting it via phosphorylation results in less susceptibility to fatigue [24]. These shifts may also be attributable to organismal differences since some studies consider mice [19, 51], while Nelson et al examine fatigue in Drosophila [24].

While SOCE plays obvious roles in $Ca^{2+}$ handling, it also regulates other intracellular processes. For instance, SOCE has been shown to regulate the fission and fusion dynamics of mitochondria [46]. Additionally, STIM1 has been shown to engage a variety of other binding partners in addition to Orai1, including POST (partner of STIM1), which facilitates its interactions with SERCA, PMCA, the $Na^+$-$K^+$ pump, and nuclear transporters [52, 53]. The multiplicity of roles for SOCE might help explain the disagreement between experimental measurements of force vs. frequency in dnOrai1 cells and predictions of our model Figure 6. For instance, changes in the mitochondrial network associated with SOCE-related mutations [54] might impact the rates of phosphate and ATP cycling in our model as well as $Ca^{2+}$ uptake in the myoplasm. As shown in Figure 6, a 50% increase in resting myoplasmic phosphate would account for the difference between model predictions and experimental measurements.

While our model incorporates many of the important players in excitation and contraction in skeletal muscle, we note some opportunities for future developments. We acknowledge that our treatment of SOCE is simplified, consisting of a single ODE governing Orai1 open probability; the detailed dynamics of STIM1 oligomerization, diffusion, and association with Orai1 may be explored in future models. However, detailed models introduce many free parameters, requiring additional experimental data for robust model calibration [55, 56]. Additionally, all of our parameters are currently estimated using data collected in single mouse myofibers at room temperature [36, 40, 41]; new datasets are needed to reliably calibrate models of human myofibers at physiological temperatures. Finally, future work is required to elucidate the spatial features of SOCE in skeletal muscle. Experimental data show that myofibers undergo

dramatic structural reorganization following exercise, including changes in the T-tubule system and assembly of CEUs [20, 57] While our model differentiates between junctional and bulk regions within the myofiber, spatial modeling approaches such as VCell [58] or SMART [59] are required to properly explore this aspect of $Ca^{2+}$ signaling in skeletal muscle. Such models provide a natural opportunity to include compartmentalization of $Ca^{2+}$ into additional organelles such as mitochondria, which serve as a $Ca^{2+}$ sink and are themselves regulated by $Ca^{2+}$ [60, 61].

Despite these limitations, our findings may have implications beyond skeletal muscle, including neurons and cardiomyocytes [18, 21, 22, 62], as well as nonexcitable cells such as immune cells [63, 64]. For example, the frequency-dependent role of SOCE explored here may naturally extend to postsynaptic signaling in neuronal dendritic spines [18, 65]. Thus, our study positions SOCE as a key regulator of SR and myoplasmic $Ca^{2+}$, particularly important for cellular events that trigger rapid store depletion.

# Materials and Methods

## Numerical implementation

The full model is described in Supplementary Information (Tables S1 to S7) and consists of 51 nonlinear ordinary differential equations. Initial conditions were estimated starting from default values of each variable (Table S4) and integrating the equations with no input current out to $t = 1000$ s in MATLAB using the stiff ODE solver, ode15s. The initial values were then either defined by the values at $t = 1000$ s or the values when the following condition was met:

$$\frac{dy_i}{dt}\frac{1}{y_{i,\text{norm}}} < 10^{-5} \text{ for } i \text{ from 1 to 51}, \tag{15}$$

where $y_i$ is the state variable associated with index $i$ and $y_{i,\text{norm}}$ is a normalizing factor for $y_i$, defined in Table S4.

In all cases, the steady-state solution with no SOCE ($g_{\text{Orai1}} = 0$) was computed before defining $K_{\text{STIM1}}$ as a fraction of the resting SR $Ca^{2+}$ concentration without SOCE (Table S7). This strategy was adopted to avoid cases with unrealistic levels of SOCE under resting conditions. Steady-state values for each state variable were then estimated for the desired Orai1 conductance ($g_{\text{Orai1}} > 0$) at the assigned value of $K_{\text{STIM1}}$, before solving the dynamics with various stimuli using ode15s. This strategy was used to compute steady-state for all variables except myoplasmic phosphate and SR phosphate, which were fixed to estimated parameter values (Table S7), and SR $Ca^{2+}$-phosphate precipitate, which was always assumed to start at 0 μM. MATLAB code from this study is freely available on Github and through Zenodo [66].

## Sensitivity Analysis

Morris sensitivity analysis was conducted using the UQLab framework in MATLAB [67]. As described in the main text, maximum and average values of myoplasmic $Ca^{2+}$ and sarcolemma voltage were used as quantities of interest (QOIs). All parameters were varied according to a uniform distribution, from 0.5 to 2 times the reference value from literature (Table S7) Morris analysis yielded the absolute value of the mean ($\mu^*$) and the standard deviation ($\sigma$) of the elementary effects. A parameter was treated as sensitive if $\mu^*$ was greater than 10% of the maximum $\mu^*$ over all parameters for that QOI.

## Parameter Estimation

To ensure good fits to both sarcolemma voltage and myoplasmic $Ca^{2+}$, we conducted parameter estimation in two stages, first calibrating the model to match physiological action potentials and then further constraining parameters to simultaneously recapitulate myoplasmic $Ca^{2+}$ and sarcolemma voltage over time. In the first step, the objective function was defined as the normalized sum of square errors between experimentally measured voltage and model predictions for the data from [41]:

$$\mathcal{F}_V = \frac{1}{N}\sum_{j=1}^{N}\left(\frac{V_{\text{SL,model}}(t_j) - V_{\text{SL,exp}}(t_j)}{\sigma_V}\right)^2, \tag{16}$$

where $V_{\mathrm{SL,model}}(t_j)$ and $V_{\mathrm{SL,exp}}(t_j)$ are, respectively, the predicted and experimentally measured sarcolemma voltage at time $t_j$. $N$ is the number of time points considered and $\sigma_V$ is the standard deviation of the measurement error (fixed at 5 mV). For this step, only parameters with greater than 10% of the maximum sensitivity index for average or peak voltage (35 parameters total, Figure 2A) were included in the fitting. Fitting was conducted using particle swarm optimization in MATLAB, with a swarm size of 30 particles and maximum stall count of 25.

In the second step, a new objective function was defined, starting with the weighted sum of square errors between experimental and simulated myoplasmic $Ca^{2+}$:

$$\mathcal{F}_{\mathrm{Ca}^{2+}} = \sum_{i=1}^{2} \left[ \mathcal{F}_{i,\mathrm{Ca}^{2+}\infty} + \frac{1}{N_i} \sum_{j=1}^{N_i} \left( \frac{[\mathrm{Ca}^{2+}]_{\mathrm{avg,model},i}(t_j) - [\mathrm{Ca}^{2+}]_{\mathrm{avg,exp},i}(t_j)}{\sigma_c} \right)^2 \right], \tag{17}$$

where $[\mathrm{Ca}^{2+}]_{\mathrm{avg,model},i}(t_j)$ and $[\mathrm{Ca}^{2+}]_{\mathrm{myo,exp},i}(t_j)$ are the predicted (defined in Equation (14)) and experimentally measured spatially averaged myoplasmic calcium concentration at time $t_j$ for experiment $i$ and $\sigma_c$ is the standard deviation of the measurement error (fixed at 0.5 μM). $\mathcal{F}_{i,\mathrm{Ca}^{2+}\infty}$ represents an additional fitting constraint for each experiment that ensures a good match with experimentally characterized myoplasmic and SR $Ca^{2+}$ at steady-state:

$$\mathcal{F}_{i,\mathrm{Ca}^{2+}\infty} = \left( \frac{[\mathrm{Ca}^{2+}]_{i,\mathrm{myo}}(t=0) - 0.1\ \mu\mathrm{M}}{0.1\ \mu\mathrm{M}} \right)^2 + \left( \frac{[\mathrm{Ca}^{2+}]_{\mathrm{SR},i}(t=0) - 500\ \mu\mathrm{M}}{500\ \mu\mathrm{M}} \right)^2 \tag{18}$$

A total objective function was constructed to ensure good fits with both $Ca^{2+}$ and voltage data simultaneously, $\mathcal{F}_V + \mathcal{F}_{\mathrm{Ca}^{2+}}$. All parameters were included in this fitting step, starting with initial guesses given by the previous estimation for applicable parameters and using the same specifications for particle swarm optimization. The final optimized values for each parameter are reported in Table S7.

## Acknowledgments

The authors would like to thank Invild Devold for her careful review and helpful feedback on our manuscript. We would also like to thank Profs. Samuel Ward, Andrew McCulloch, and Simon Schenk for insightful conversations on skeletal muscle biology and exercise.

Simulation results presented in this paper benefited from the Triton Shared Computing Cluster at the San Diego Supercomputer Center [68]. This work was supported in part by the Wu Tsai Human Performance Alliance at the University of California, San Diego (to P.R.). E.A.F. is supported by the National Science Foundation under grant EEC-2127509 to the American Society for Engineering Education and by the Wu Tsai Human Performance Alliance.

## Declaration of Interests

P.R. is a consultant for Simula Research Laboratory in Oslo, Norway and receives income. The terms of this arrangement have been reviewed and approved by the University of California, San Diego in accordance with its conflict-of-interest policies.

## References

[1] Thomas K. Uchida and Scott L. Delp. *Biomechanics of Movement: The Science of Sports, Robotics, and Rehabilitation*. MIT Press, Jan. 12, 2021. 396 pp. ISBN: 978-0-262-04420-2. Google Books: Hu8OEAAAQBAJ.

[2] Kavitha Mukund and Shankar Subramaniam. "Skeletal Muscle: A Review of Molecular Structure and Function, in Health and Disease". In: *WIREs Systems Biology and Medicine* 12.1 (2020), e1462. ISSN: 1939-005X.

[3] Pedro M. Rodríguez Cruz, Judith Cossins, David Beeson, and Angela Vincent. "The Neuromuscular Junction in Health and Disease: Molecular Mechanisms Governing Synaptic Formation and Homeostasis". In: *Frontiers in Molecular Neuroscience* 13 (Dec. 3, 2020), p. 610964. ISSN: 1662-5099. pmid: 33343299.

[4] Roger M. Enoka and Jacques Duchateau. "Rate Coding and the Control of Muscle Force". In: *Cold Spring Harbor Perspectives in Medicine* 7.10 (Oct. 2017), a029702. ISSN: 2157-1422. pmid: 28348173.

[5] A. J. Fuglevand, D. A. Winter, and A. E. Patla. "Models of Recruitment and Rate Coding Organization in Motor-Unit Pools". In: *Journal of Neurophysiology* 70.6 (Dec. 1, 1993), pp. 2470–2488. ISSN: 0022-3077, 1522-1598.

[6] A. R. Pucci, L. Griffin, and E. Cafarelli. "Maximal Motor Unit Firing Rates during Isometric Resistance Training in Men". In: *Experimental Physiology* 91.1 (Jan. 2006), pp. 171–178. ISSN: 0958-0670. pmid: 16210447.

[7] W. Ament, G. J. Bonga, A. L. Hof, and G. J. Verkerke. "EMG Median Power Frequency in an Exhausting Exercise". In: *Journal of Electromyography and Kinesiology: Official Journal of the International Society of Electrophysiological Kinesiology* 3.4 (1993), pp. 214–220. ISSN: 1050-6411. pmid: 20870536.

[8] Juan C. Calderón, Pura Bolaños, and Carlo Caputo. "The Excitation–Contraction Coupling Mechanism in Skeletal Muscle". In: *Biophysical Reviews* 6.1 (Jan. 24, 2014), pp. 133–160. ISSN: 1867-2450. pmid: 28509964.

[9] Jared Talbot and Lisa Maves. "Skeletal Muscle Fiber Type: Using Insights from Muscle Developmental Biology to Dissect Targets for Susceptibility and Resistance to Muscle Disease". In: *Wiley interdisciplinary reviews. Developmental biology* 5.4 (July 2016), pp. 518–534. ISSN: 1759-7684. pmid: 27199166.

[10] Paul R. Shorten, Paul O'Callaghan, John B. Davidson, and Tanya K. Soboleva. "A Mathematical Model of Fatigue in Skeletal Muscle Force Contraction". In: *Journal of Muscle Research and Cell Motility* 28.6 (Aug. 2007), pp. 293–313. ISSN: 0142-4319, 1573-2657.

[11] Arthur J. Cheng, Nicolas Place, and Håkan Westerblad. "Molecular Basis for Exercise-Induced Fatigue: The Importance of Strictly Controlled Cellular $Ca^{2+}$ Handling". In: *Cold Spring Harbor Perspectives in Medicine* 8.2 (Feb. 2018), a029710. ISSN: 2157-1422.

[12] David G. Allen and Sofie Trajanovska. "The Multiple Roles of Phosphate in Muscle Fatigue". In: *Frontiers in Physiology* 3 (Dec. 11, 2012), p. 463. ISSN: 1664-042X. pmid: 23248600.

[13] Feliciano Protasi, Laura Pietrangelo, and Simona Boncompagni. "Calcium Entry Units (CEUs): Perspectives in Skeletal Muscle Function and Disease". In: *Journal of Muscle Research and Cell Motility* 42.2 (June 2021), pp. 233–249. ISSN: 0142-4319, 1573-2657.

[14] Patrick G Hogan and Anjana Rao. "Store-Operated Calcium Entry: Mechanisms and Modulation". In: *Biochemical and biophysical research communications* 460.1 (Apr. 24, 2015), pp. 40–49. ISSN: 0006-291X. pmid: 25998732.

[15] Yukio Furukawa, Shunsuke Teraguchi, Takahisa Ikegami, Onur Dagliyan, Lin Jin, Damien Hall, Nikolay V. Dokholyan, Keiichi Namba, Shizuo Akira, Tomohiro Kurosaki, Yoshihiro Baba, and Daron M. Standley. "Intrinsic Disorder Mediates Cooperative Signal Transduction in STIM1". In: *Journal of Molecular Biology* 426.10 (May 15, 2014), pp. 2082–2097. ISSN: 0022-2836.

[16] Paul J. Hoover and Richard S. Lewis. "Stoichiometric Requirements for Trapping and Gating of Ca2+ Release-Activated Ca2+ (CRAC) Channels by Stromal Interaction Molecule 1 (STIM1)". In: *Proceedings of the National Academy of Sciences* 108.32 (Aug. 9, 2011), pp. 13299–13304.

[17] Riina M. Luik, Bin Wang, Murali Prakriya, Minnie M. Wu, and Richard S. Lewis. "Oligomerization of STIM1 Couples ER Calcium Depletion to CRAC Channel Activation". In: *Nature* 454.7203 (July 24, 2008), pp. 538–542. ISSN: 1476-4687. pmid: 18596693.

[18] Kanishka Basnayake, David Mazaud, Lilia Kushnireva, Alexis Bemelmans, Nathalie Rouach, Eduard Korkotian, and David Holcman. "Nanoscale Molecular Architecture Controls Calcium Diffusion and ER Replenishment in Dendritic Spines". In: *Science Advances* 7.38 (Sept. 17, 2021), eabh1376. ISSN: 2375-2548.

[19] Lan Wei-LaPierre, Ellie M. Carrell, Simona Boncompagni, Feliciano Protasi, and Robert T. Dirksen. "Orai1-Dependent Calcium Entry Promotes Skeletal Muscle Growth and Limits Fatigue". In: *Nature Communications* 4.1 (Nov. 18, 2013), p. 2805. ISSN: 2041-1723.

[20] Simona Boncompagni, Antonio Michelucci, Laura Pietrangelo, Robert T. Dirksen, and Feliciano Protasi. "Exercise-Dependent Formation of New Junctions That Promote STIM1-Orai1 Assembly in Skeletal Muscle". In: *Scientific Reports* 7.1 (Oct. 27, 2017), p. 14286. ISSN: 2045-2322.

[21] E.È. Saftenku. "Simulation of Store-Operated Calcium Entry in Neurons". In: *Neurophysiology* 54.1 (Jan. 1, 2022), pp. 14–24. ISSN: 1573-9007.

[22] Julia Hermes, Vesela Borisova, and Jens Kockskämper. "Store-Operated Calcium Entry Increases Nuclear Calcium in Adult Rat Atrial and Ventricular Cardiomyocytes". In: *Cells* 12.23 (Nov. 23, 2023), p. 2690. ISSN: 2073-4409. pmid: 38067118.

[23] Xaver Koenig, Rocky H. Choi, Klaus Schicker, Daniel P. Singh, Karlheinz Hilber, and Bradley S. Launikonis. "Mechanistic Insights into Store-Operated Ca2+ Entry during Excitation-Contraction Coupling in Skeletal Muscle". In: *Biochimica et Biophysica Acta (BBA) - Molecular Cell Research*. 15th European Symposium on Calcium 1866.7 (July 1, 2019), pp. 1239–1248. ISSN: 0167-4889.

[24] Marin E Nelson, Benjamin L Parker, James G Burchfield, Nolan J Hoffman, Elise J Needham, Kristen C Cooke, Timur Naim, Lykke Sylow, Naomi XY Ling, Deanne Francis, Dougall M Norris, Rima Chaudhuri, Jonathan S

Oakhill, Erik A Richter, Gordon S Lynch, Jacqueline Stöckli, and David E James. "Phosphoproteomics Reveals Conserved Exercise-stimulated Signaling and AMPK Regulation of Store-operated Calcium Entry". In: *The EMBO Journal* 39.8 (Apr. 15, 2020), e104246. ISSN: 0261-4189. pmid: 32291792.

[25] W. Wallinga, S. L. Meijer, M. J. Alberink, M. Vliek, E. D. Wienk, and D. L. Ypey. "Modelling Action Potentials and Membrane Currents of Mammalian Skeletal Muscle Fibres in Coherence with Potassium Concentration Changes in the T-tubular System". In: *European Biophysics Journal* 28.4 (May 25, 1999), pp. 317–329. ISSN: 0175-7571, 1432-1017.

[26] Sageanne Senneff and Madeleine M. Lowery. "Effects of Extracellular Potassium on Calcium Handling and Force Generation in a Model of Excitation-Contraction Coupling in Skeletal Muscle". In: *Journal of Theoretical Biology* 519 (June 2021), p. 110656. ISSN: 00225193.

[27] M.B. Cannell and D.G. Allen. "Model of Calcium Movements during Activation in the Sarcomere of Frog Skeletal Muscle". In: *Biophysical Journal* 45.5 (May 1984), pp. 913–925. ISSN: 00063495.

[28] S. C. Cannon, R. H. Brown, and D. P. Corey. "Theoretical Reconstruction of Myotonia and Paralysis Caused by Incomplete Inactivation of Sodium Channels". In: *Biophysical Journal* 65.1 (July 1993), pp. 270–288. ISSN: 0006-3495. pmid: 8396455.

[29] N. B. Standen and P. R. Stanfield. "Inward Rectification in Skeletal Muscle: A Blocking Particle Model". In: *Pflugers Archiv: European Journal of Physiology* 378.2 (Dec. 28, 1978), pp. 173–176. ISSN: 0031-6768. pmid: 310542.

[30] Anamika Dayal, Kai Schrötter, Yuan Pan, Karl Föhr, Werner Melzer, and Manfred Grabner. "The Ca2+ Influx through the Mammalian Skeletal Muscle Dihydropyridine Receptor Is Irrelevant for Muscle Performance". In: *Nature Communications* 8.1 (Sept. 7, 2017), p. 475. ISSN: 2041-1723.

[31] E Ríos, M Karhanek, J Ma, and A González. "An Allosteric Model of the Molecular Interactions of Excitation-Contraction Coupling in Skeletal Muscle." In: *The Journal of general physiology* 102.3 (Sept. 1, 1993), pp. 449–481. ISSN: 0022-1295, 1540-7748.

[32] Gaia Butera, Denis Vecellio Reane, Marta Canato, Laura Pietrangelo, Simona Boncompagni, Feliciano Protasi, Rosario Rizzuto, Carlo Reggiani, and Anna Raffaello. "Parvalbumin Affects Skeletal Muscle Trophism through Modulation of Mitochondrial Calcium Uptake". In: *Cell Reports* 35.5 (May 4, 2021), p. 109087. ISSN: 2211-1247.

[33] Robyn M. Murphy, Noni T. Larkins, Janelle P. Mollica, Nicole A. Beard, and Graham D. Lamb. "Calsequestrin Content and SERCA Determine Normal and Maximal $Ca^{2+}$ Storage Levels in Sarcoplasmic Reticulum of Fast- and Slow-twitch Fibres of Rat". In: *The Journal of Physiology* 587.2 (Jan. 15, 2009), pp. 443–460. ISSN: 0022-3751, 1469-7793.

[34] Leonardo Nogueira, Natalie K. Gilmore, and Michael C. Hogan. "Role of Parvalbumin in Fatigue-Induced Changes in Force and Cytosolic Calcium Transients in Intact Single Mouse Myofibers". In: *Journal of Applied Physiology* 132.4 (Mar. 3, 2022), p. 1041. pmid: 35238653.

[35] Stephen M. Baylor and Stephen Hollingworth. "Intracellular Calcium Movements during Excitation–Contraction Coupling in Mammalian Slow-Twitch and Fast-Twitch Muscle Fibers". In: *Journal of General Physiology* 139.4 (Apr. 1, 2012), pp. 261–272. ISSN: 1540-7748, 0022-1295.

[36] Stephen M. Baylor and Stephen Hollingworth. "Simulation of Ca2+ Movements within the Sarcomere of Fast-Twitch Mouse Fibers Stimulated by Action Potentials". In: *Journal of General Physiology* 130.3 (Sept. 1, 2007), pp. 283–302. ISSN: 1540-7748, 0022-1295.

[37] D G Allen and H Westerblad. "Role of Phosphate and Calcium Stores in Muscle Fatigue". In: *The Journal of Physiology* 536 (Pt 3 Nov. 1, 2001), pp. 657–665. ISSN: 0022-3751. pmid: 11691862.

[38] M W Fryer, V J Owen, G D Lamb, and D G Stephenson. "Effects of Creatine Phosphate and P(i) on Ca2+ Movements and Tension Development in Rat Skinned Skeletal Muscle Fibres." In: *The Journal of Physiology* 482.1 (1995), pp. 123–140. ISSN: 1469-7793.

[39] Andrew T. Dolan and Scott L. Diamond. "Systems Modeling of Ca2+ Homeostasis and Mobilization in Platelets Mediated by IP3 and Store-Operated Ca2+ Entry". In: *Biophysical Journal* 106.9 (May 6, 2014), pp. 2049–2060. ISSN: 0006-3495. pmid: 24806937.

[40] Oscar A. Rincón, Andrés F. Milán, Juan C. Calderón, and Marco A. Giraldo. "Comprehensive Simulation of Ca2+ Transients in the Continuum of Mouse Skeletal Muscle Fiber Types". In: *International Journal of Molecular Sciences* 22.22 (Nov. 17, 2021), p. 12378. ISSN: 1422-0067.

[41] Daniel R. Miranda, Eric Reed, Abdulrahman Jama, Michael Bottomley, Hongmei Ren, Mark M. Rich, and Andrew A. Voss. "Mechanisms of Altered Skeletal Muscle Action Potentials in the R6/2 Mouse Model of Huntington's Disease". In: *American Journal of Physiology. Cell Physiology* 319.1 (July 1, 2020), pp. C218–C232. ISSN: 1522-1563. pmid: 32432924.

[42] *PlotDigitizer: Extract Data from Graph Image Online*. PlotDigitizer. URL: https://plotdigitizer.com/ (visited on 04/09/2025).

[43] Max D. Morris. "Factorial Sampling Plans for Preliminary Computational Experiments". In: *Technometrics* 33.2 (May 1, 1991), pp. 161–174. ISSN: 0040-1706.

[44] Camille Rabesahala de Meritens, Amado Carreras-Sureda, Nicolas Rosa, Robert Pick, Christoph Scheiermann, and Nicolas Demaurex. "STIM1/2 Maintain Signaling Competence at ER-PM Contact Sites during Neutrophil Spreading". In: *Journal of Cell Biology* 224.5 (Mar. 21, 2025), e202406053. ISSN: 0021-9525.

[45] D. G. Allen, G. D. Lamb, and H. Westerblad. "Skeletal Muscle Fatigue: Cellular Mechanisms". In: *Physiological Reviews* 88.1 (Jan. 2008), pp. 287–332. ISSN: 0031-9333.

[46] Jinliang Nan, Jiamin Li, Yinuo Lin, Muhammad Saif Ur Rahman, Zhengzheng Li, and Lingjun Zhu. "The Interplay between Mitochondria and Store-operated Ca2+ Entry: Emerging Insights into Cardiac Diseases". In: *Journal of Cellular and Molecular Medicine* 25.20 (Oct. 2021), pp. 9496–9512. ISSN: 1582-1838. pmid: 34564947.

[47] Samuel R. Hamner and Scott L. Delp. "Muscle Contributions to Fore-Aft and Vertical Body Mass Center Accelerations over a Range of Running Speeds". In: *Journal of biomechanics* 46.4 (Feb. 22, 2013), pp. 780–787. ISSN: 0021-9290. pmid: 23246045.

[48] Minnie M. Wu, Riina M. Luik, and Richard S. Lewis. "Some Assembly Required: Constructing the Elementary Units of Store-Operated Ca2+ Entry". In: *Cell Calcium.* New Developments in Ca2+ Influx Channels and Their Regulation 42.2 (Aug. 1, 2007), pp. 163–172. ISSN: 0143-4160.

[49] Ilya Grigoriev, Susana Montenegro Gouveia, Babet van der Vaart, Jeroen Demmers, Jeremy T. Smyth, Srinivas Honnappa, Daniël Splinter, Michel O. Steinmetz, James W. Putney, Casper C. Hoogenraad, and Anna Akhmanova. "STIM1 Is a Microtubule plus End Tracking Protein Involved in Remodeling of the Endoplasmic Reticulum". In: *Current biology : CB* 18.3 (Feb. 12, 2008), pp. 177–182. ISSN: 0960-9822. pmid: 18249114.

[50] Yi-Chun Yeh, Yu-Ping Lin, Holger Kramer, and Anant B Parekh. "Single-Nucleotide Polymorphisms in Orai1 Associated with Atopic Dermatitis Inhibit Protein Turnover, Decrease Calcium Entry and Disrupt Calcium-Dependent Gene Expression". In: *Human Molecular Genetics* 29.11 (July 21, 2020), pp. 1808–1823. ISSN: 0964-6906.

[51] Zui Pan, Dongmei Yang, Ramakrishnan Y. Nagaraj, Thomas A. Nosek, Miyuki Nishi, Hiroshi Takeshima, Heping Cheng, and Jianjie Ma. "Dysfunction of Store-Operated Calcium Channel in Muscle Cells Lacking Mg29". In: *Nature Cell Biology* 4.5 (May 2002), pp. 379–383. ISSN: 1476-4679.

[52] Grigory Krapivinsky, Luba Krapivinsky, Stephanie C. Stotz, Yunona Manasian, and David E. Clapham. "POST, Partner of Stromal Interaction Molecule 1 (STIM1), Targets STIM1 to Multiple Transporters". In: *Proceedings of the National Academy of Sciences* 108.48 (Nov. 29, 2011), pp. 19234–19239.

[53] Robert Hooper, Elsie Samakai, Joseph Kedra, and Jonathan Soboloff. "Multifaceted Roles of STIM Proteins". In: *Pflugers Archiv : European journal of physiology* 465.10 (Oct. 2013), pp. 1383–1396. ISSN: 0031-6768. pmid: 23568369.

[54] Helen E. Collins, Lan He, Luyun Zou, Jing Qu, Lufang Zhou, Silvio H. Litovsky, Qinglin Yang, Martin E. Young, Richard B. Marchase, and John C. Chatham. "Stromal Interaction Molecule 1 Is Essential for Normal Cardiac Homeostasis through Modulation of ER and Mitochondrial Function". In: *American Journal of Physiology-Heart and Circulatory Physiology* 306.8 (Apr. 15, 2014), H1231–H1239. ISSN: 0363-6135.

[55] Nathaniel J. Linden, Boris Kramer, and Padmini Rangamani. "Bayesian Parameter Estimation for Dynamical Models in Systems Biology". In: *PLOS Computational Biology* 18.10 (Oct. 21, 2022). Ed. by Jeffrey J. Saucerman, e1010651. ISSN: 1553-7358.

[56] Lingxia Qiao, Ali Khalilimeybodi, Nathaniel J. Linden-Santangeli, and Padmini Rangamani. "The Evolution of Systems Biology and Systems Medicine: From Mechanistic Models to Uncertainty Quantification". In: *Annual Review of Biomedical Engineering* 27 (Volume 27, 2025 May 1, 2025), pp. 425–447. ISSN: 1523-9829, 1545-4274.

[57] Tanya R. Cully, Robyn M. Murphy, Llion Roberts, Truls Raastad, Robert G. Fassett, Jeff S. Coombes, Izzy Jayasinghe, and Bradley S. Launikonis. "Human Skeletal Muscle Plasmalemma Alters Its Structure to Change Its Ca2+-Handling Following Heavy-Load Resistance Exercise". In: *Nature Communications* 8.1 (Feb. 13, 2017), p. 14266. ISSN: 2041-1723.

[58] Ann E. Cowan, Ion I. Moraru, James C. Schaff, Boris M. Slepchenko, and Leslie M. Loew. "Spatial Modeling of Cell Signaling Networks". In: *Methods in Cell Biology.* Vol. 110. Elsevier, 2012, pp. 195–221. ISBN: 978-0-12-388403-9.

[59] Emmet A. Francis, Justin G. Laughlin, Jørgen S. Dokken, Henrik N. T. Finsberg, Christopher T. Lee, Marie E. Rognes, and Padmini Rangamani. "Spatial Modeling Algorithms for Reactions and Transport in Biological Cells". In: *Nature Computational Science* (Dec. 19, 2024), pp. 1–14. ISSN: 2662-8457.

[60] A. Leung, D. Ohadi, G. Pekkurnaz, and P. Rangamani. "Systems Modeling Predicts That Mitochondria ER Contact Sites Regulate the Postsynaptic Energy Landscape". In: *npj Systems Biology and Applications* 7.1 (June 2, 2021), p. 26. ISSN: 2056-7189.

[61] Carlotta Giorgi, Saverio Marchi, and Paolo Pinton. "The Machineries, Regulation and Cellular Functions of Mitochondrial Calcium". In: *Nature Reviews Molecular Cell Biology* 19.11 (Nov. 2018), pp. 713–730. ISSN: 1471-0080.

[62] Lorena Benedetti, Ruolin Fan, Aubrey V. Weigel, Andrew S. Moore, Patrick R. Houlihan, Mark Kittisopikul, Grace Park, Alyson Petruncio, Philip M. Hubbard, Song Pang, C. Shan Xu, Harald F. Hess, Stephan Saalfeld, Vidhya Rangaraju, David E. Clapham, Pietro De Camilli, Timothy A. Ryan, and Jennifer Lippincott-Schwartz. "Periodic ER-plasma Membrane Junctions Support Long-Range Ca2+ Signal Integration in Dendrites". In: *Cell* 188.2 (Jan. 23, 2025), 484–500.e22. ISSN: 1097-4172. pmid: 39708809.

[63] R. A. Clemens and C. A. Lowell. "Store-Operated Calcium Signaling in Neutrophils". In: *J Leukoc Biol* 98.4 (Oct. 2015), pp. 497–502. ISSN: 1938-3673 (Electronic) 0741-5400 (Linking). PMID: 25714804.

[64] Monika Vig and Jean-Pierre Kinet. "Calcium Signaling in Immune Cells". In: *Nature Immunology* 10.1 (Jan. 2009), pp. 21–27. ISSN: 1529-2916.

[65] Nikolai C. Dembrow and William J. Spain. "Input Rate Encoding and Gain Control in Dendrites of Neocortical Pyramidal Neurons". In: *Cell reports* 38.7 (Feb. 15, 2022), p. 110382. ISSN: 2211-1247. pmid: 35172157.

[66] Anusha Kumar, Emmet A. Francis, and Juliette Hamid. *RangamaniLabUCSD/SkelMuscleCa: V1.0.1*. Version v1.0.1. Zenodo, May 21, 2025.

[67] Stefano Marelli and Bruno Sudret. "UQLab: A Framework for Uncertainty Quantification in Matlab". In: (July 7, 2014), pp. 2554–2563.

[68] San Diego Supercomputer Center. *Triton Shared Computing Cluster*. 2022. Pre-published.